Toward surfaces with droplet impact robustness and low contact angle hysteresis

*Wenwu Ding Carlos A. Dorao Maria Fernandino**

Address: Department of Energy and Process Engineering, Norwegian University of Science and Technology, Trondheim, Norway
Email Address: maria.fernandino@ntnu.no

Keywords: *droplet impact, structure shape, hysteresis, robustness, wetting*

Superhydrophobic surfaces show excellent water repellent performance. However, liquid impalement occurs when a droplet impacts on the surface at high velocity. To achieve higher resistance to liquid impalement at the same scale, a dense array of structures or structures with pinning at the structures top are typically used, but they also lead to increased contact angle hysteresis and higher energy dissipation. Changing the structure side wall shape can help to maintain low hysteresis and withstand high impact energy at the same scale.

Droplet contact angle, contact angle hysteresis and droplet impact experiments are performed on both conical and cylindrical pillar surfaces. Comparing conical and cylindrical pillar structures with the same pitch and height, we found that cylindrical pillars exhibit higher critical Weber number but result in larger contact angle hysteresis and larger liquid residue size when above a critical Weber number. A proper design of conical structures can maintain large contact angle, low hysteresis, strong resistance to impalement, higher number of bouncings and smaller liquid residue size. In addition, the critical Weber number for the conical structures in this work is higher than micro-patterned pillar surfaces at the same pitch range, implying that we improve the anti-wetting performance further.

1 Introduction

Achieving superhydrophobicity is crucial to various applications, such as anti-wetting, [1] anti-icing surfaces, [2,3] controlled droplet transport, [4,5] self-cleaning [6–11] and heat and mass transfer in phase change processes. [12–15] One way of producing a super-hydrophobic surface is by the combination of a hydrophobic coating and a roughness design. [16] It is normally defined as superhydrophobic if the apparent contact angle is larger than 150° and the contact angle hysteresis is smaller than 10°. [16] However, it is sometimes suggested that superhydrophobicity should comprise not only high contact angle and low contact angle hysteresis but also the bouncing ability, where the number of bouncings [17] and the ability to avoid a Cassie-Wenzel transition during droplet impact [18] is frequently stressed. It has been shown that above a threshold impacting velocity, the Cassie-Wenzel transition can happen when the liquid touches the cavity bottom or reaches the local advancing contact angle. [19–21] To increase this critical velocity, the surface structure has to be designed such that it imposes a strong resistance to liquid impalement. Without changing the structure scale, this target can be realized by using a dense array of structures [19–24] or structures with special top to pin the liquid. For instance, sharp edge structures [25] can resist impalement better due to the additional pinning effect. On the other hand, a dense array or a special pinning top leads to a higher contact angle hysteresis due to the extra pinning, which goes against the desired properties of superhydrophobic surfaces.

The whole bouncing process includes different phases: the drop falling down to first contact with the surface, spreading to a maximum contact diameter, receding back and moving backward into the air. It has been shown that the dynamic contact angle can affect the drop impact behavior, [26–29] especially during the receding stage, which also affects the energy dissipation. Different criteria for the occurrence of droplet rebound have been reported in the literature, based on droplet impacting energy, [30] receding contact angle and contact angle hysteresis. [26,27] In order to have a rebound, the energy dissipation (i.e. viscous dissipation [30,31] and contact angle hysteresis [30,31])

has to be minimised. Viscous dissipation can be reduced by minimizing the solid-liquid contact area. To further reduce energy dissipation and to increase the number of bouncings, the contact angle hysteresis needs to be reduced as well, which requires a surface design with less dense and lower pinning structures. However, a less dense surface structure with less pinning on the structures top will enhance liquid penetration and result in higher adhesion forces, limiting the surface robustness towards droplet bouncing.

In this sense, optimization of anti-impalement ability and contact angle hysteresis is conflicting. While dense structures or pinning top can have better anti-impalement ability, the contact angle hysteresis in these cases is increased, thus increasing the energy dissipation and reducing the chances of bouncing. The main way to increase the anti-impalement ability while maintaining a low contact angle hysteresis has been achieved either by reducing the structures scale, namely the use of nano-structures, or by increasing the hierarchical level. [22,32]

We present another solution to decouple the combined effect of anti-impalement ability and contact angle hysteresis. We experimentally study droplet impact on conical structured surfaces with different conical geometries. We demonstrate that by changing the geometrical parameters of the conical structures, we are able to relax the conflict between low contact angle hysteresis and anti-impalement ability, obtaining surfaces allowing droplet bouncing even at high droplet impact velocity.

Conical structures show high contact angle, low contact angle hysteresis and at the same time, certain level of anti-impalement capability, [33,34] due to their low solid-liquid contact area and no distinct pinning effect on the conical structures top. By varying the distance between the cones and the cones apex angle, the penetration of liquid is avoided. [34] As opposed to what happens with pillar-like structures that enhance pinning of the contact line on the pillars top, [25] conical structures do not show strong pinning effect and maintain a low contact angle hysteresis even at small pitch distances. [34] On the other hand, in the absence of pinning on the structures top, liquid will tend to penetrate and the anti-impalement ability will be affected, especially at higher droplet impact velocities. After penetration, liquid residue might exist. It is shown in previous work that the liquid residue size is increased when the surface tension is decreased [35] or when the impact velocity is increased. [36] In a lattice Boltzmann simulation, [37] the impact velocity effect is observed as well. They proposed that the energy dissipation is strong when the liquid is withdrawn from the post, thus the number of impaled posts can affect the impact outcome. However, it has been reported that mono-stable Cassie surfaces can initiate a Wenzel-Cassie transition and thus the penetrated liquid can move away from the structure. [38] Unfortunately, a mono-stable Cassie surface still shows partial rebound when below a certain temperature. The lower the temperature, the larger the wetted area inside the structure, where the increased adhesion is due to condensation. In the literature, [39] liquid flow behavior both above and also within the structures is reported to influence the impact outcome. For the same surface, the volume flow inside the structure is increased when Weber number is higher. At higher Weber numbers, they observe that liquid flow inside the grooves dominates, while at low Weber numbers, the flow above the structures dominates. Compared with cylindrical structures, conical structures have negligible adhesion and therefore less energy dissipation is expected when liquid flows above the structures top. Besides, the enlarged side wall of conical surfaces is expected to impede the liquid flow inside the structures and thus reduce the wetted area.

In this work, we experimentally study droplet impact on conical structured surfaces with different conical geometries. We compare the performance of conical structures against similar cylindrical pillar structured surfaces to investigate the role of the side wall shape. We demonstrate that by changing the geometrical parameters of the conical structures, we are able to relax the conflict between low contact angle hysteresis and anti-impalement ability, obtaining surfaces allowing droplet

bouncing even at high droplet impact velocity. In addition, we quantify and compare the liquid residue size when a drop impacts above the critical Weber number (i.e when the droplet impact starts to show partial rebound). Conical structures have lower resistance to liquid penetration but they present less liquid residue size, which is suitable for reduction of liquid residue accumulation. In short, the novelty of this work is a new solution presented here for relaxing the conflict between low contact angle hysteresis and anti-impalement ability and also a method to reduce liquid residue size.

2 Results and discussion

The detail sample fabrication and experimental process are presented in the experimental section. In general, we produce conical samples and cylindrical samples and characterize their wetting properties and their droplet impact behaviors. In the text below, the following abbreviation is used for the conical pillars: CP3H12 indicates cones with pitch 3 μm and height 12 μm, and the same holds for the other samples, CP5H12, CP812, CP10H12, CP3H20, CP5H20, CP8H20 and CP10H20. For the cylindrical pillar surfaces, SP3H12 is the abbreviation for pillars with pitch 3 μm and height 12 μm, and similarly for SP5H12, SP8H12 and SP10H12. The pillar structures have diameter of ~ 1.7 μm. The scanning electron microscope (SEM) images are shown in Figure 1(a). The experimental setup is shown in Figure 1(b). The apparent contact angle is shown in Table 1. In Table 2, we summarize the contact angle hysteresis data for the conical and cylindrical pillar surfaces.

Table 1. Apparent contact angle of water on conical and cylindrical pillar surfaces

Sample	*Cone* 12 μm	*Cone* 20 μm	*Pillar* 12 μm
Pitch 3 μm	174 ± 3°	174 ± 1°	146 ± 5°
Pitch 5 μm	173 ± 1°	175 ± 1°	159 ± 1°
Pitch 8 μm	175 ± 2°	175 ± 1°	163 ± 1°
Pitch 10 μm	172 ± 1°	174 ± 1°	165 ± 2°

Table 2. Contact angle hysteresis of water on conical and cylindrical pillar surfaces

Sample	*Cone* 12 μm	*Cone* 20 μm	*Pillar* 12 μm
Pitch 3 μm	8 ± 3°	5 ± 3°	45 ± 2°
Pitch 5 μm	7 ± 2°	5 ± 1°	25 ± 1°
Pitch 8 μm	5 ± 3°	5 ± 3°	19 ± 3°
Pitch 10 μm	9 ± 5°	5 ± 4°	12 ± 3°

Here we show the detailed droplet impact process at Weber number We=2.8 ($We = \frac{\rho R V^2}{\gamma}$, ρ is density, V is impact velocity, γ is surface tension, R is droplet radius), for the surfaces with cylindrical pillars and conical structures, all with pitch 3 μm and height 12 μm, SP3H12 and CP3H12 for short, respectively. As shown in Figure 2(a) (green patch), CP3H12 has low contact angle hysteresis with sliding angle (which is defined as the tilting angle when a droplet starts to slide) around 0.5°, while SP3H12 has much higher hysteresis with sliding angle of 47°. The droplet volume for these two cases is 6-7 μl in the tilting experiment.

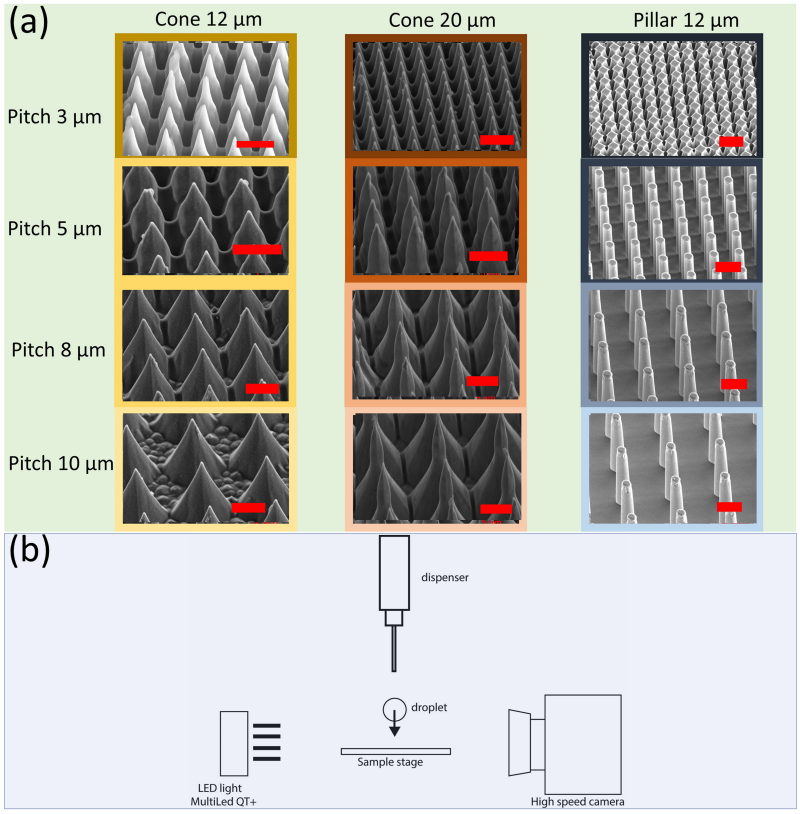

Figure 1. (a) SEM images of produced samples. All scale bars are 5 μm. (b) Impact experiment set up.

Figure 2(b) (blue patch) shows snapshot images of drop impact at We=2.8, Reynolds number Re= 470 ($Re = \frac{\rho RV}{\mu}$, μ is liquid dynamic viscosity), Capillary number Ca=0.005 (Ca=$\mu V/\gamma$) and Bond number Bo=0.16 ($Bo = \frac{\rho g R^2}{\gamma}$, g is gravitational acceleration). Figure 2(c) (yellow patch) presents the evolution of the wetted baseline size for the same experiments in Figure 2(b). As shown in Figure 2 (b) and (c), CP3H12 displays faster bouncing process, while the impact process of SP3H12 has a longer contact time. Previous works show that entrapped gas can produce wettability independent bouncing [40] at certain low velocity condition. But the impact difference from Figure 2 (b) shows that the cases here are not in the wettability independent regime as the impact velocity is larger, around 3.78 m/s to 0.45 m/s. As the Weber number here is quite small, all cases show clean rebound, and we expect to have little or no droplet penetration into the structure. The contact time during the whole process is longer for the larger hysteresis surface, with the main difference during the receding stage. This is consistent with the reported effect of wettability on droplet spreading and receding for flat surfaces for wettability ranging from hydrophilic to hydrophobic. [41–43] The spreading process is governed by inertia, [44,45] thus there is no distinct difference. However, in the receding stage, the surface tension forces are driving the liquid backward, while viscous force and possible contact line pinning force are resisting the movement. The slower receding speed for the case of the cylindrical pillar surface SP3H12 is attributed to larger surface adhesion as compared to the conical structures in the surface CP3H12, which leads to a slower starting of the receding (conical case starts to recede at around 4 ms while cylindrical case starts around 6 ms due to higher contact angle hysteresis) and slower motion during the receding. In addition, in the case of cylindrical structures, the pinning of the liquid on the top of the structures adds an extra contribution to the resistance force. Therefore, the total resistance

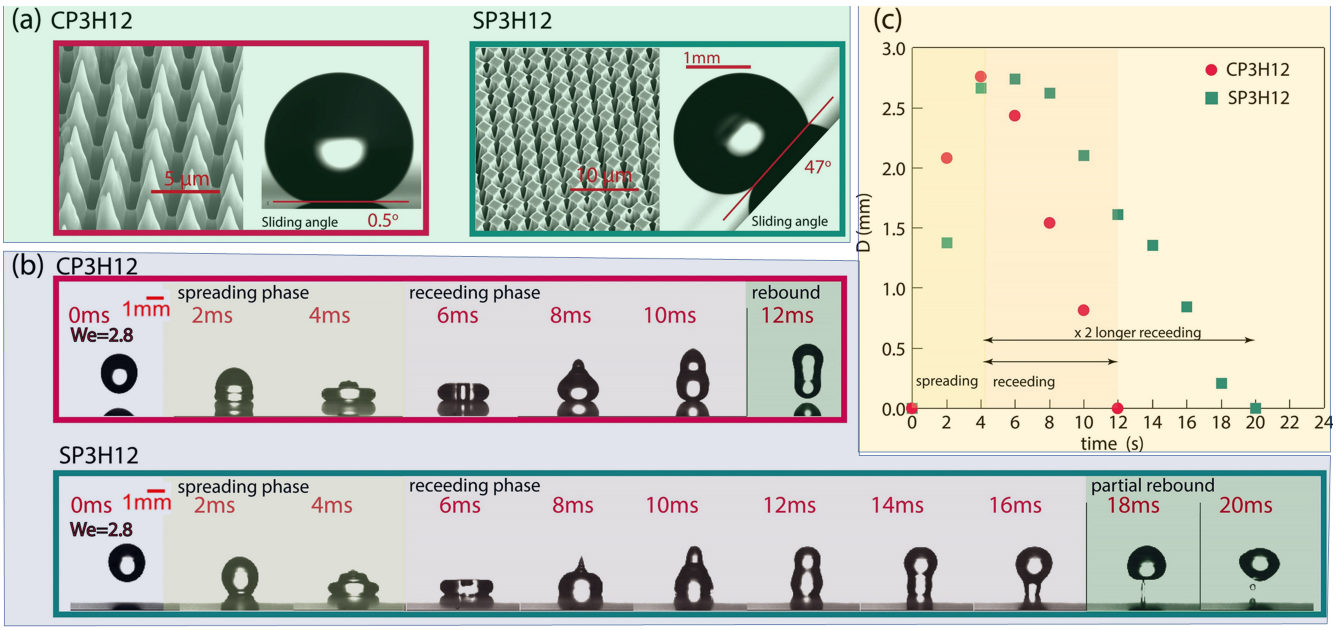

Figure 2. Drop impact at small Weber number ($We = 2.8$) for conical and cylindrical structured surfaces (all with pitch 3 μm and height 12 μm). (a) SEM image of fabricated cones and pillars. The droplet on cone surface slides around 0.5°. The droplet on cylindrical surface starts to slide at around 47°. (b) Drop impact images for CP3H12 and SP3H12. The cylindrical case displays much larger receding time. The pinnig effect of high sliding angle case retards liquid movement. A small pinned drop appears at 18 ms, which is out of the surface in the next frame. (c) Plot of wetted contact baseline for CP3H12 and SP3H12 as a function of time. The SP3H12 surface has much larger hysteresis and shows slower receding process.

force is larger and the liquid recoils in a slower way. At around 18 ms (just after the droplet has lifted off from the surface), there is a small amount of liquid pinning on the surface. However, this pinned droplet is not in Wenzel state, since it leaves the surface in the next frame. As this is a low Weber number impact condition, no distinct penetration is expected. This indicates that the liquid is temporally pinned on the surface due to higher resistance force.

Figure 3(a) shows the receding time (the time from starting of receding to complete rebound) vs. contact angle hysteresis. This figure illustrates that the receding process is slowed down when the hysteresis is higher. The cones height has negligible effect here, which is probably due to the low We number, and the liquid has no distinct penetration into the structure. For these drop impact cases, inertia and capillary forces are the same (namely impact velocity and surface tension are the same), and Ca number ($\mu V/\gamma$) is around 0.005 for this low viscosity liquid. Therefore we can assume that viscosity is not dominant here and the difference in receding time is mainly due to the contact angle hysteresis. This implies that hysteresis plays an important role in the impact process. Lower contact angle hysteresis leads to a faster receding process, consistent with previous results for smooth surfaces. [27] In addition, pinning on the surface adds an extra resistance during the receding process and affects the lift off of the droplet. The rate of energy dissipation per unit length at the contact line during the advancing and receding stages can be expressed as [46, 47]

$$W_A = U\gamma_{LV}(cos(\theta_E) - cos(\theta_A)) \quad (1)$$

$$W_R = U\gamma_{LV}(cos(\theta_R) - cos(\theta_E)) \quad (2)$$

respectively, for quasi-static conditions, where θ_E is the equilibrium contact angle, θ_A is the advancing contact angle, θ_R is the receding contact angle, U is liquid velocity and γ_{LV} is the liquid-vapour

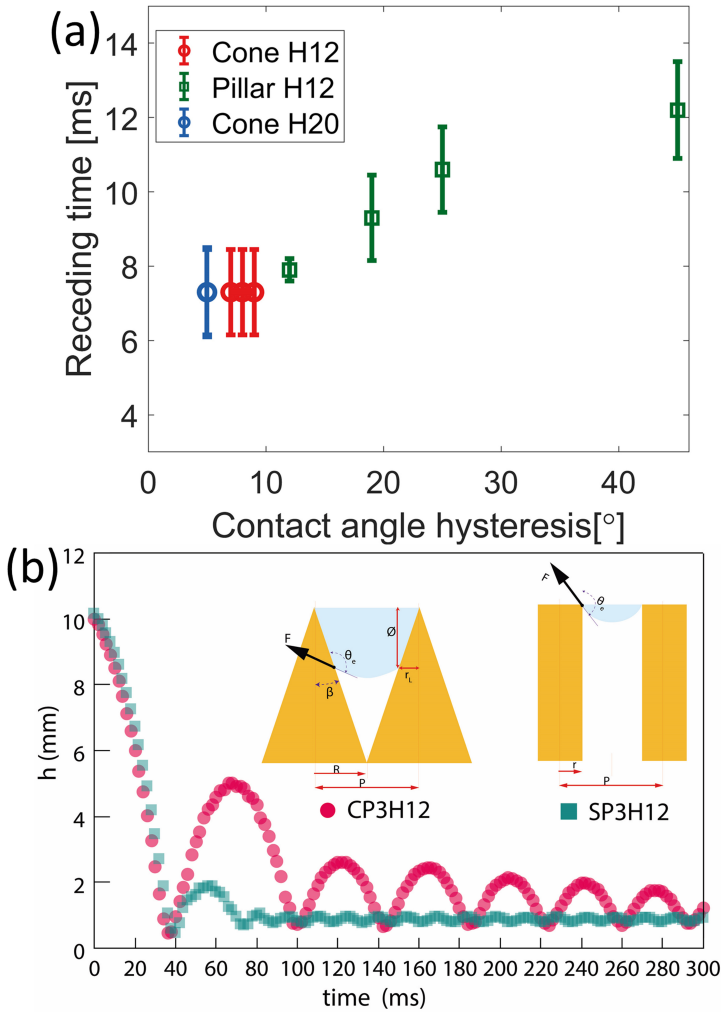

Figure 3. (a) Comparison of the receding time for cones and pillars at We=2.8. The higher hysteresis case has longer receding time.(b) Drop bouncing process at We = 2.8 for CP3H12 and SP3H12 surfaces. The height h (droplet center height) in the y-axis represents the droplet center position. The higher hysteresis pillar surface (45 ± 2°) only shows one bouncing, while the the conical structures surface (8 ± 3°) has multiple bouncings. In the subplot, β is the cone half apex angle, P is the pitch, R is the cone bottom radius, ϕ is the penetration depth fraction, θ_e is the intrinsic angle.

surface tension. During the advancing and receding stages, the contact angle is not at its equilibrium value θ_E and this irreversibility causes dissipation. In order to reduce this type of energy loss, hysteresis has to be minimized. In summary, lower contact angle hysteresis benefits drop impact process by showing lower energy dissipation.

Figure 3(b) shows the droplet center position as a function of time for surfaces CP3H12 and SP3H12 at impact We=2.8, Re=470, Ca=0.005, Bo=0.16. Both droplets are released from the same distance above the surface. Once the droplet meets the surface it starts spreading, reaches a maximum diameter and then starts to recede. If the droplet energy is larger than all the energy dissipation, the droplet lifts off from the surface completely.

It is seen in Figure 3(b) that the first bouncing is much higher for CP3H12 compared with SP3H12, which means there is more energy dissipation for the latter one. This is attributed to the higher solid-liquid contact area and the larger pinning effect in the case of pillar structures. In addition, the droplet on the SP3H12 surface only shows one bouncing and then remains stuck

to the surface, while on the CP3H12 surface, the droplet presents multiple bouncings. This result indicates that energy dissipation is quite large in the former case and thus the droplet energy after the first bouncing is lower than the energy dissipation in the second contact process, which results in a non-bouncing condition. This pinning effect for surface SP3H12 is also evident in Figure 2(b), which is attributed to the edge of the pillars top, where pinning effects contribute further to energy loss. [46,47] In Figure 3(b), it is schematically shown how the pinning at the top of the structures can affect the liquid penetration depth. In the case of the conical structures, the liquid can penetrate a distance ϕ into the structures (with half apex angle β, intrinsic angle θ_e, wetted radius r) since pinning is low at the cones top. On the other hand, in the case of the cylindrical pillars, liquid is not able to penetrate so much within the structures due to the high pinning on the cylinder edges. While this would imply that cylindrical pillars present a stronger resistance to liquid penetration, at the same time the pinning effect at the top of the structures will introduce an extra resistance for a droplet to leave the surface.

As shown in the previous sections, cones show small contact angle hysteresis, faster solid-liquid contact process and higher number of bouncings as compared to pillars at low *We* number. At higher *We* numbers conical structures are less resistant to liquid penetration during droplet impact, as shown in Figure 4. At *We*=9, *Re*=843, *Ca*=0.01, *Bo*=0.16, a water droplet is able to bounce from both surfaces. However, as the impact We number is increased (*We*=40, *Re*=1778, *Ca*=0.02, *Bo*=0.16), the cylindrical pillar surface SP5H12 shows complete rebound whereas a small amount of liquid remains after the partial bouncing on the surface CP5H12 with conical structures. This can be explained by the increased pillar top size and also possibly the pinning of the liquid at the top edge of the cylindrical pillars, which resists better the liquid penetration into the structures. Cylindrical pillar structures show a higher threshold impact velocity than conical structures with the same pitch and height before transitioning from complete to partial rebound at higher We numbers.

If the cones and pillars have the same top, the conical structures can show better anti-wetting properties, which is supported in Figure 5, where we compare truncated cones (static contact angle $162 \pm 2^\circ$, contact angle hysteresis $25 \pm 2^\circ$) and cylindrical pillars (static contact angle $160 \pm 2^\circ$, contact angle hysteresis $26 \pm 3^\circ$) with similar top feature for the same pitch and height. The results demonstrate that the truncated cones surface has complete rebound at (*We*=9, *Re*=843, *Ca*=0.01, *Bo*=0.16) while the cylindrical pillar case exhibits partial rebound. Consequently, the sidewall shape also affects the anti-wetting ability. On the other hand, as it has been discussed in the previous sections, the pinning of the liquid at the bigger top of the cylindrical structures results in higher contact angle hysteresis and therefore longer solid-liquid contact time, resulting in more droplet adhesion at lower *We* numbers. Sharper conical structures are able to maintain a low contact angle hysteresis for different geometrical parameters (see Table 2), namely pitch and height, and can therefore be designed to obtain a satisfying surface for droplet impact at higher velocity without compromising the low contact angle hysteresis property. In order to achieve both low hysteresis and larger anti-wetting ability, we need to design the conical structures geometry accordingly. In this way, one expects to have a surface with higher bouncing ability both at low and high impact *We* numbers.

Depending on the *We* number, wettability and roughness, [1,26–28,48] different droplet impact regimes can be observed. In particular, the partial rebound regime, where some liquid remains attached to the surface after the bouncing, is against our anti-wetting target. The breakthrough pressure $P_{0,bk}$, [49] which is the critical pressure difference that induces the breakthrough scenario, can be used to estimate the resistance to impalement. This critical pressure can be estimated by establishing a force balance (similar to Jurin's law [50]) between the wetting liquid pressure force

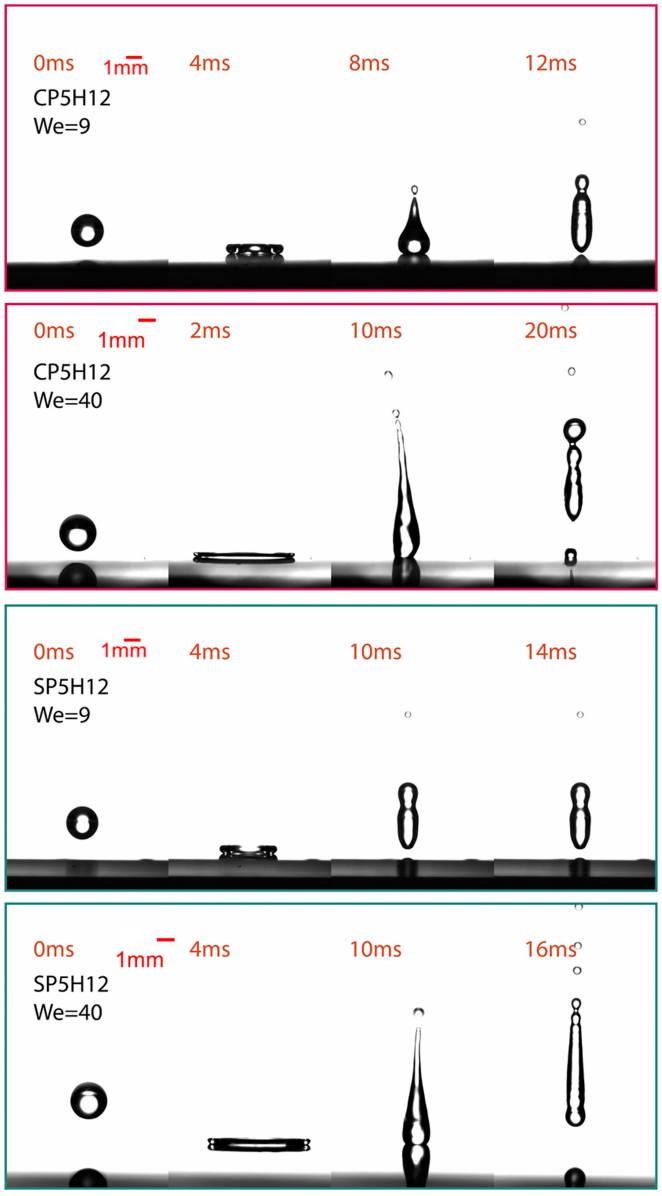

Figure 4. At We=9, both CP5H12 and SP5H12 show complete rebound. At We=40, CP5H12 exhibits partial rebound, while SP5H12 displays complete rebound. Cylindrical pillars resist more the liquid penetration.

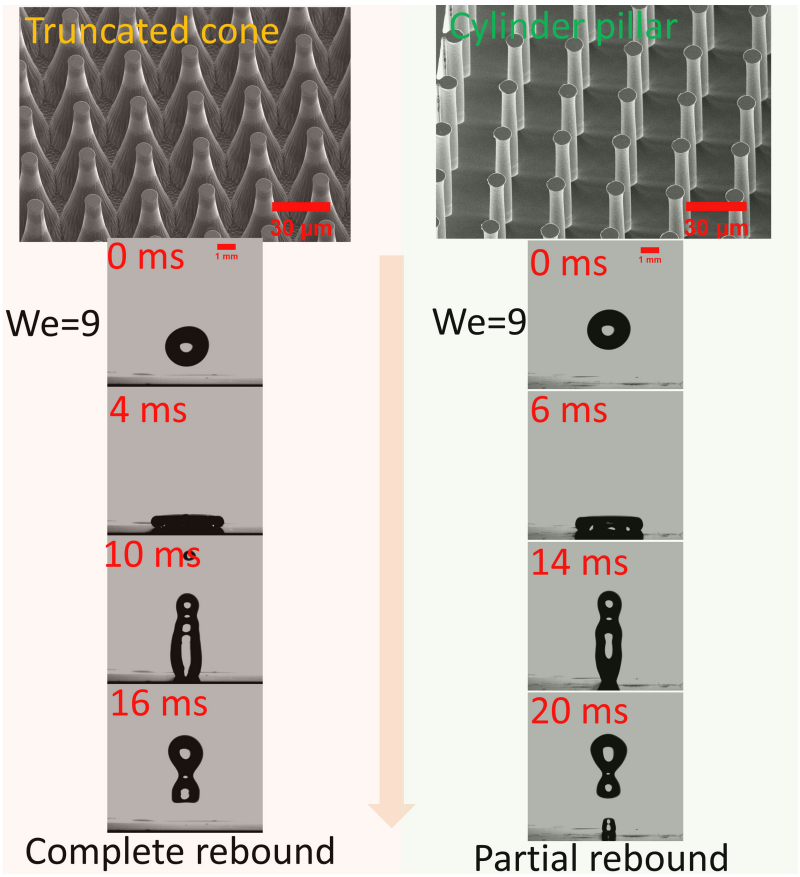

Figure 5. Drop impact on truncated cones (left) and cylindrical pillars (right) with similar pillar top, all with pitch 30 μm, height 40 μm. At We=9, truncated cones show complete rebound, while cylindrical pillars show partial rebound. The truncated cones have static contact angle 162 $\pm$ 2° and contact angle hysteresis 25 $\pm$ 2°, cylindrical pillars show static contact angle 160 $\pm$ 2° and contact angle hysteresis 26 $\pm$ 3°.

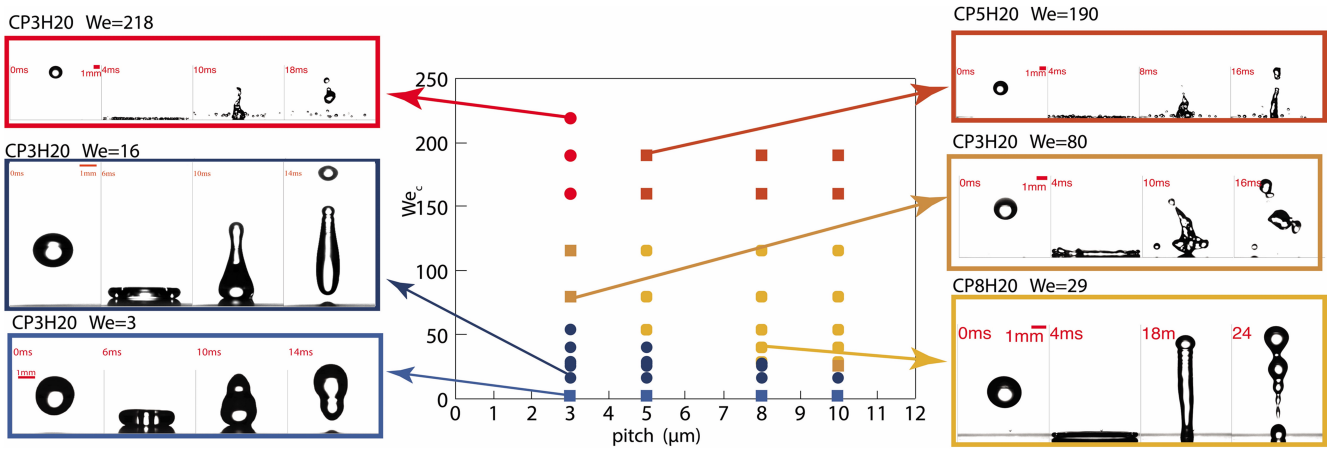

Figure 6. Impact regime for cones with height 20 μm. In the middle, the Weber number is plotted as a function of the cone pitch distance. On the left, three impact cases are shown; from top to bottom: fragmentation/splash without liquid residue, rebound with satellite droplet and complete rebound. On the most right hand side, three impact cases are shown; from top to bottom: fragmentation/splash with liquid residue, rebound with major droplet splitting and partial rebound.

and the anti-wetting capillary force, namely

$$P_{0,L}A + 2\pi r_L \gamma_{LV} \cos(\theta_A - \beta) = 0 \tag{3}$$

The wetting force from the drop impact is the product of the liquid pressure $P_{0,L}$ and the acting area A. The capillary force acting around the wetted perimeter $2\pi r_L$ is acting to resist the liquid penetration. At an assumed penetration ϕ (as pictured in Figure 3), the contact area becomes $A = P^2 - \pi r_L^2$, when considering the droplet on a unit cell where P is the pitch distance. Using this new area in equation (3) and looking for the critical pressure when $P_{0,L} = P_{0,bk}$, one gets

$$P_{0,bk} = \frac{-\pi P \phi \gamma_{LV} \cos(\theta_A - \beta)}{P^2 - P^2 \pi \phi^2 / 4} \tag{4}$$

for the breakthrough pressure for conical structures of pitch P and half apex angle β. Thus, to avoid a wetting transition, increasing of the breakthrough pressure can be achieved by reducing the pitch P and the half apex angle.

In this section, we show drop impact results for cones with 20 μm height with the same pitch design as mentioned previously. By keeping the pitch constant and increasing the height, the half apex angle is varied. As a result, cones can be designed to reach the same impact performance as pillar structures without increasing the contact angle hysteresis.

The impact outcome for the range of tested impact *We* numbers vs. cones pitch is shown in Figure 6 for cones with height 20 μm *We*=3-218, *Re*=486-4151, *Ca*=0.005-0.05, *Bo*=0.16). By increasing the impact *We* number, the droplet on CP3H20 shows complete rebound, rebound with satellite droplet, rebound with major droplet splitting and fragmentation/splash without liquid residue. For pitch $5\mu m$, $8\mu m$ and $10\mu m$, the regime consists of complete rebound, rebound with satellite droplet, rebound with liquid residue and fragmentation/splash with liquid residue. With increasing Weber number, the larger pitch cone samples start to show partial rebound after the first bouncing. As shown here, surface CP3H20 can achieve no-residue state even at *We* number as high as around 218. At this *We* number, the droplet will splash away and the small droplets roll off easily due to the low hysteresis. As the cone height is increased and the pitch is fixed, the apex angle is reduced. This result is qualitatively in agreement with the modeling of the breakthrough pressure, which is higher for smaller cones apex angle.

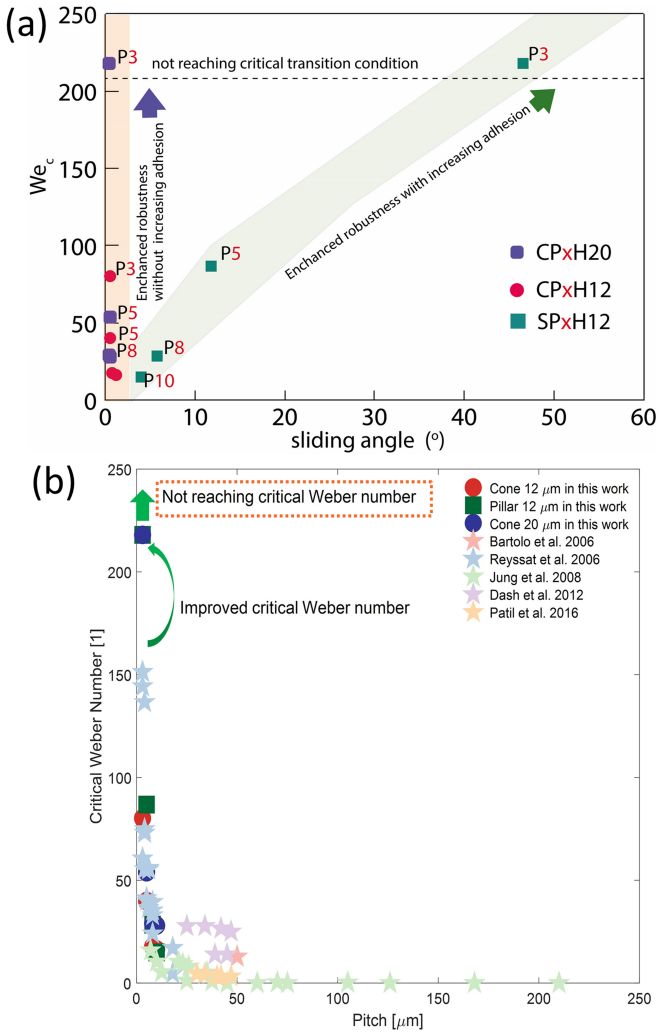

Figure 7. (a) Critical Weber number as a function of sliding angle for all cases tested. At $We = 218$, the two cases show still clean rebound, while all other cases start to show liquid residue.(b) Critical Weber number is plotted vs. pitch distance, for surfaces in this work and other micro-scale pillar array surfaces found in literature. [19–21, 23, 51] Data range is confined to water drop falling perpendicular to rigid micro-patterned substrates

Figure 7(a) shows the critical Weber number for transition from total to partial rebound for all tested conical and cylindrical surfaces characterized by their corresponding sliding angle. As shown here, the critical Weber number for cylindrical pillared surfaces increases with higher sliding angle. In this case, the diameter and height of the pillars remain constant. The conical structured surfaces show increasing critical Weber number without any increase in adhesion. The increase of the critical Weber number is achieved by reducing the pitch which in turn reduces the apex angle of the cones (for constant cones height). It is possible to see that for the same height of the structures, pillars show higher critical Weber number than cones. However, if the height of the cones is increased or their apex angle is decreased, equivalent performance is obtained. Figure 7(a) demonstrates that conical structures can decouple hysteresis and anti-impalement ability. This decoupling makes conical structures a good path for maintaining high contact angle, low hysteresis, high number of bouncings and high resistance to liquid impalement. Figure 7(b) summarizes the critical Weber number in this work and other data found in literature for micro-patterned rigid surfaces with pitch in the range of 3 μm - 230 μm. [19–21, 23, 51] From this plot, the conical pillars surface with pitch 3 μm and height 20 μm performs better than the cited works.

To further check the remaining liquid residue property, we use a Keyence (VHX-950F) microscope to view the surface from the top after the drop impact. In order to know the wetted area, we remove the upper part of the liquid by approaching a tissue paper to the top of the droplet. In Figure 11 of supplemental file, we present the top view liquid residue before and after the drop impact for selected cases.

In Figure 8(a), we plot the critical Weber number vs. the breakthrough pressure $P_{0,bk}$. The equation of $P_{0,bk}$ is shown in equation (4). The same way is used to derive the expression for the breakthrough pressure $P_{0,bkp}$ for the cylindrical pillars, which results in $P_{0,bkp} = \frac{-2\pi r_p \gamma_{LV} \cos\theta_A}{P^2 - \pi r_P^2}$ for the cylindrical case. The r_p is the cylindrical pillar radius. To calculate breakthrough pressure for the cones, we need to assume a penetration depth fraction for ϕ. In Figure 8(a), we presents $P_{0,bk}$ data for ϕ=0.1 (yellow patch), ϕ=0.3 (red patch) and ϕ=0.5 (brown patch) together with $P_{0,bkp}$ for the cylindrical case (green patch). Generally, it is observed that the critical We number is larger when $P_{0,bk}$ is higher.

The liquid residue size from the image processing of the experiments described in Figure 11 in the supplementary file (those above the critical *We* number) is shown in Figure 8(b), (c) and (d). The impact condition can be described by the *We* number. For the same surface, the larger the Weber number above the critical Weber number We_c, the more liquid residue it has due to the higher impact energy, which is shown in Figure 8(b) for three We cases (We=81, We=137, We=218). The x axis is $(We\text{-}We_c)/We_c$, which reflects how many times the difference between impact Weber number and critical Weber number $(We\text{-}We_c)$ is over the critical Weber number We_c (this data is shown in Figure 7 (a)). Figure 8(b) clearly indicates that the case of cylindrical pillars (distributed around the green line) has larger liquid residue size compared with conical pillar cases (distributed around red line).

Apart from *We* number, the liquid residue size can be different at the same We number for different surfaces. We propose that this is related with the structure ability to resist penetration and also to resist liquid lateral movement inside the structures after penetration. The residue size is plotted vs. $P_{0,bk}$ assuming ϕ=0.3 for the conical case in Figure 8(c). As shown in the Figure, the liquid residue area decreases with $P_{0,bk}$ for both cylindrical (green patch) and conical cases (red patch) at We=137, while similar to Figure 8(b), the cylindrical case has larger liquid residue size compared with the conical case. Figure 8(c) indicates that surface anti-penetration ability does affect the liquid residue size.

In addition, the ability of the liquid to move laterally inside the structure is proposed to be linked with the parameter R_{SA}, which is defined as the open lateral area divided by the whole lateral area in one unit structure space. The schematic drawing of R_{SA} is shown in Figure 8(e). For the conical case, $R_{SA} = (P*H - P*H/2)/(P*H)$=0.5, while for the cylindrical pillar case, $R_{SA} = (P*H - D*H)/(P*H) = 1 - D/P$. The higher the R_{SA}, the easier the liquid moves in the lateral direction inside the structure due to larger open space. The liquid residue size at We=137 is plotted vs. R_{SA} in Figure 8(d), where the trend supports the view that the lateral movement ability is related with the liquid residue size. Therefore, we conclude that the conical structures have less resistance to penetration (Figure 4) but they have much better ability to resist liquid lateral movement, which is further supported in Figure 8(f).

The difference in liquid residue area is related with the actual wetted area inside the structure. It is proposed that the liquid can wet more the cylindrical pillars than the conical ones. We check the spreading ability inside the structure by recording the behavior of a low surface tension ethanol droplet. In Figure 8(f), we deposit an ethanol droplet onto CP10H12 and SP10H12 in order to see how liquid behaves at Wenzel state conditions, which can provide information about the liquid behavior inside the structure. We observe a pinned drop on the conical case but a spreading drop for the cylinder case. We illustrate that the liquid flow inside the cones experiences more resistance,

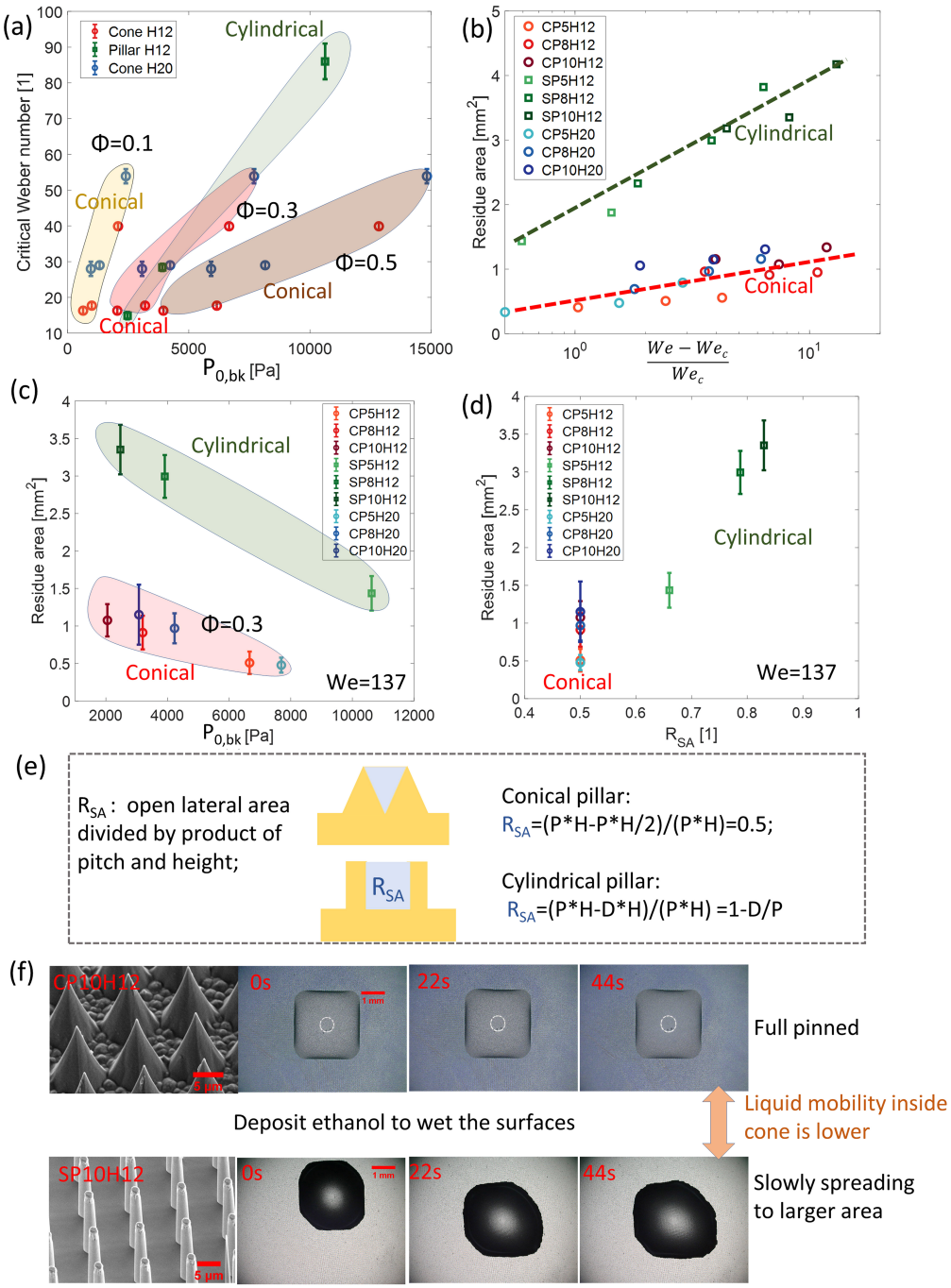

Figure 8. In (a), critical Weber number of conical and cylindrical cases is plotted vs. breakthrough pressure $P_{0,bk}$. For cones, three cases using ϕ=0.1, ϕ=0.3, ϕ=0.5 are shown. In (b), the top view liquid residue area is plotted with $(We\text{-}We_c)/We_c$. In (c), the top view liquid residue area is plotted vs. $P_{0,bk}$ at We=137. ϕ=0.3 is used for conical cases. In (d), the top view liquid residue area is plotted vs. R_{SA} at We=137. In (e), a schematic demonstration of R_{SA} in 2-D is presented. In (f), comparison of liquid mobility on CP10H12 and SP10H12 by depositing an ethanol drop on the surface.

which is possibly one of the reasons that there is less wetted area. Even when the spreading of an ethanol droplet is different from the water impact case, we believe that the difference of liquid mobility inside the conical structures and cylindrical pillars is reflected in such indirect experiment as we use the same liquid on the same target surfaces. Combining the critical Weber number and the liquid residue results, we conclude that conical structures show better anti-wetting ability both at low Weber number (Cassie case) and at higher Weber number (partial Wenzel or Wenzel case).

3 Conclusions

In this work, we reported that conical structured surfaces with low hysteresis and high apparent contact angle can reach a high critical We number for a complete rebound of an impacting droplet. The change of the structure sidewall shape, namely the design of conical shape, can maintain a low pinning effect but a high anti-impalement ability. The results suggest that an appropriate design of the cones can increase the critical *We* number for complete rebound. Surfaces with cylindrical pillars have also been studied, but contrary to the conical structures, the increase of the critical *We* number is at the cost of increasing the contact angle hysteresis. In addition, we observe less liquid residue size when above the critical Weber number for the conical case. Here, we advance this field by providing a method to decouple contact angle hysteresis and anti-impalement ability at the same scale, namely by designing of the structure side wall shape, in addition to previous methods like structures down-scaling or increasing the hierarchical level. [22,32] We experimentally reveal how anti-wetting properties are affected by structure side wall shape. As summarized in Figure 7(b), the critical Weber number in this work can be higher than the ones in literature for micro-patterned rigid surfaces [19–21,23,51] with the same pitch range, which means that the anti-impalement ability is improved further. The study of the structure sidewall topography on the anti-wetting properties provides more insights into superhydrophobic surfaces design. Visualization of the liquid interface between conical structures can further advance the development in this regard.

4 Experimental Section

Tilting experiment and contact angle. The surface wetting properties for water are characterized by the apparent contact angle and contact angle hysteresis. The contact angle is measured using an optical tensiometer from Biolin Scientific at ambient conditions. A de-ionized water droplet with volume 4-8 μl is deposited gently onto the sample and the static contact angle is obtained (see Table 1). For the contact angle hysteresis, the surface is tilted while we record the process until the droplet starts to slide. In Table 2, the contact angle hysteresis data for the conical and cylindrical pillar surfaces are shown. The advancing angle, receding angle and tilting angle are provided in supplemental file.

Droplet impact. A syringe is used to dispense a free-fall liquid droplet (with volume around 4-10 μl) at a given height above the tested surface. The droplet impact process is recorded using a Photron Fastcam SA3 camera with 500 frames per second at ambient conditions. The impact velocity is adjusted by varying the distance of the syringe to the surface, obtaining a range of impacting Weber numbers from around 2 to 218, capillary number number from 0.005 to 0.05, Reynolds number from 470 to 4151, Bond number around 0.16, where the droplet radius and droplet velocity (largest velocity during first impact process) are obtained from image processing in Matlab. During the experiment, the distance of the syringe to the surface is increased until the partial rebound regime (i.e. lift off of the impinging droplet with some liquid residue on the surface) is observed. When this is the case, the needle is lowered step by step to find the height

condition at which the partial rebound is first observed. This is defined as the critical distance, and thus critical impacting velocity and critical Weber number for this surface.

Surface fabrication. A silicon wafer is rinsed in solvent, acetone, ethanol, isopropanol, and deionized water and further dried with N_2 gas. The sample is next coated with negative photoresist Mr-dwl-5 at 3000 rpm for 30 s and prebaked (50 $^{\circ}C$ for 5 minutes, then 90 $^{\circ}C$ for 5 minutes and another 5 minutes at 50 $^{\circ}C$). Next, we expose the photoresist using MLA150 (Heidelberg Instruments) with a laser wavelength of 405 nm as the beam. The wafer is patterned with circular dots of 1 micrometer in diameter, pitch 3 μm, 5μm, 8μm and 10 μm, and etched in an Oxford Cryo ICP-RIE dry etching device with SF_6/O_2 and CHF_3. By changing the etching parameters, three types of samples are obtained: conical pillars with height 12 μm, conical pillars with height 20 μm and cylindrical pillars with height 12 μm. The etching parameters for the cones with height 12 μm are: the etching temperature is -50 °C, in a SF_6/O_2-85/16 sccm gas, at a pressure of 50 mTorr during 10 minutes, followed by O_2 plasma during 10 min, then CHF_3 for 5 minutes. The etching parameters for the cones with height 20 μm are the same, except that the etching in SF_6/O_2 is done for 14 minutes at a pressure of 30 mTorr. The etching parameters for the cylindrical pillars are: etching temperature of -100 °C, in a SF_6/O_2-85/11 sccm gas, at a pressure of 20 mTorr during 9 minutes, then O_2 plasma for 15 minutes, and followed by CHF_3 plasma for 5 minutes. All the samples are treated with silane (Trichloro(1H,1H,2H,2H-perfluorooctyl)silane, Sigma-Aldrich) to make the samples superhydrophobic.

Acknowledgements

The Research Council of Norway is acknowledged for the support to the Norwegian Micro- and Nano-Fabrication Facility, NorFab, project number 295864.

Conflict of Interest

The authors declare that they have no conflicts of interest.

References

[1] A. Yarin, *Annual Review of Fluid Mechanics* **2006**, *38*, 1 159.

[2] L. Cao, A. K. Jones, V. K. Sikka, J. Wu, D. Gao, *Langmuir* **2009**, *25*, 21 12444.

[3] P. Guo, Y. Zheng, M. Wen, C. Song, Y. Lin, L. Jiang, *Advanced Materials* **2012**, *24*, 19 2642.

[4] C. Liu, I. Legchenkova, L. Han, W. Ge, C. Lv, S. Feng, E. Bormashenko, Y. Liu, *Langmuir* **2021**, *37*, 5 1948.

[5] C. Liu, I. Legchenkova, L. Han, W. Ge, C. Lv, S. Feng, E. Bormashenko, Y. Liu, *Langmuir* **2020**, *36*, 32 9608.

[6] X. Yao, Q. Chen, L. Xu, Q. Li, Y. Song, X. Gao, D. Quéré, L. Jiang, *Advanced Functional Materials* **2010**, *20*, 4 656.

[7] S. Nishimoto, B. Bhushan, *RSC Adv.* **2013**, *3*, 3 671.

[8] K. Liu, L. Jiang, *Annual Review of Materials Research* **2012**, *42*, 1 231.

[9] R. Blossey, *Nature Materials* **2003**, *2*, 5 301.

[10] Y. Lu, S. Sathasivam, J. Song, C. R. Crick, C. J. Carmalt, I. P. Parkin, *Science* **2015**, *347*, 6226 1132.

[11] D. Wang, Q. Sun, M. J. Hokkanen, C. Zhang, F. Y. Lin, Q. Liu, S. P. Zhu, T. Zhou, Q. Chang, B. He, Q. Zhou, L. Chen, Z. Wang, R. H. Ras, X. Deng, *Nature* **2020**, *582*, 7810 55.

[12] X. Chen, J. A. Weibel, S. V. Garimella, *Advanced Materials Interfaces* **2015**, *2*, 3 1400480.

[13] X. Chen, J. Wu, R. Ma, M. Hua, N. Koratkar, S. Yao, Z. Wang, *Advanced Functional Materials* **2011**, *21*, 24 4617.

[14] N. Miljkovic, R. Enright, Y. Nam, K. Lopez, N. Dou, J. Sack, E. N. Wang, *Nano Letters* **2013**, *13*, 1 179.

[15] K. Rykaczewski, A. T. Paxson, M. Staymates, M. L. Walker, X. Sun, S. Anand, S. Srinivasan, G. H. McKinley, J. Chinn, J. H. J. Scott, K. K. Varanasi, *Scientific Reports* **2014**, *4*, 1 1.

[16] D. Quéré, *Annual Review of Materials Research* **2008**, *38*, 1 71.

[17] C. R. Crick, I. P. Parkin, *Chemical Communications* **2011**, *47*, 44 12059.

[18] M. Nosonovsky, B. Bhushan, *Journal of Physics Condensed Matter* **2008**, *20*, 39.

[19] M. Reyssat, A. Pépin, F. Marty, Y. Chen, D. Quéré, *Europhysics Letters* **2006**, *74*, 2 306.

[20] D. Bartolo, F. Bouamrirene, Verneuil, A. Buguin, P. Silberzan, S. Moulinet, *Europhysics Letters* **2006**, *74*, 2 299.

[21] Y. C. Jung, B. Bhushan, *Langmuir* **2008**, *24*, 12 6262.

[22] K. Smyth, A. Paxon, H.-m. Kwon, T. Deng, K. K. Varanasi, In *2010 12th IEEE Intersociety Conference on Thermal and Thermomechanical Phenomena in Electronic Systems*. IEEE, ISBN 978-1-4244-5342-9, **2010** 1–8, URL `http://ieeexplore.ieee.org/document/5501329/`.

[23] N. D. Patil, R. Bhardwaj, A. Sharma, *Experimental Thermal and Fluid Science* **2016**, *74* 195.

[24] L. K. Malla, N. D. Patil, R. Bhardwaj, A. Neild, *Langmuir* **2017**, *33*, 38 9620.

[25] S. Moulinet, D. Bartolo, *European Physical Journal E* **2007**, *24*, 3 251.

[26] C. Antonini, A. Amirfazli, M. Marengo, *Physics of Fluids* **2012**, *24*, 10.

[27] C. Antonini, F. Villa, I. Bernagozzi, A. Amirfazli, M. Marengo, *Langmuir* **2013**, *29*, 52 16045.

[28] I. Malavasi, F. Veronesi, A. Caldarelli, M. Zani, M. Raimondo, M. Marengo, *Langmuir* **2016**, *32*, 25 6255.

[29] Z. Wang, C. Lopez, A. Hirsa, N. Koratkar, *Applied Physics Letters* **2007**, *91*, 2.

[30] T. Mao, D. C. Kuhn, H. Tran, *AIChE Journal* **1997**, *43*, 9 2169.

[31] R. Rioboo, M. Marengo, C. Tropea, *Experiments in Fluids* **2002**, *33* 112.

[32] C. Frankiewicz, D. Attinger, *Nanoscale* **2016**, *8*, 7 3982.

[33] K. C. Park, H. J. Choi, C. H. Chang, R. E. Cohen, G. H. McKinley, G. Barbastathis, *ACS Nano* **2012**, *6*, 5 3789.

[34] W. Ding, M. Fernandino, C. A. Dorao, *Applied Physics Letters* **2019**, *115*, 5 053703.

[35] S. Baek, H. S. Moon, W. Kim, S. Jeon, K. Yong, *Nanoscale* **2018**, *10*, 37 17842.

[36] X. Deng, F. Schellenberger, P. Papadopoulos, D. Vollmer, H. J. Butt, *Langmuir* **2013**, *29*, 25 7847.

[37] J. Hyväluoma, J. Timonen, *Journal of Statistical Mechanics: Theory and Experiment* **2009**, *2009*, 6 P06010.

[38] S. Shi, S. Shi, C. Lv, C. Lv, Q. Zheng, Q. Zheng, Q. Zheng, *Soft Matter* **2020**, *16*, 23 5388.

[39] D. Sivakumar, K. Katagiri, T. Sato, H. Nishiyama, *Physics of Fluids* **2005**, *17*, 10 100608.

[40] J. De Ruiter, R. Lagraauw, D. Van Den Ende, F. Mugele, *Nature Physics* **2015**, *11*, 1 48.

[41] J. Fukai, Y. Shiiba, T. Yamamoto, O. Miyatake, D. Poulikakos, C. M. Megaridis, Z. Zhao, *Physics of Fluids* **1995**, *7*, 2 236.

[42] Šikalo, H. D. Wilhelm, I. V. Roisman, S. Jakirlić, C. Tropea, *Physics of Fluids* **2005**, *17*, 6 1.

[43] I. S. BAYER, C. M. MEGARIDIS, *Journal of Fluid Mechanics* **2006**, *558* 415.

[44] D. C. Vadillo, A. Soucemarianadin, C. Delattre, D. C. Roux, *Physics of Fluids* **2009**, *21*, 12 1.

[45] A. Alizadeh, V. Bahadur, S. Zhong, W. Shang, R. Li, J. Ruud, M. Yamada, L. Ge, A. Dhinojwala, M. Sohal, *Applied Physics Letters* **2012**, *100*, 11 11601.

[46] D. Bonn, J. Eggers, J. Indekeu, J. Meunier, *Reviews of Modern Physics* **2009**, *81*, 2 739.

[47] Y. Xu, X. Fang, X. Su, Z. Zhou, W. Chen, *Nuclear Engineering and Design* **2012**, *253* 86.

[48] P. Tsai, M. H. W. Hendrix, R. R. M. Dijkstra, L. Shui, D. Lohse, *Soft Matter* **2011**, *7*, 24 11325.

[49] R. Hensel, R. Helbig, S. Aland, H. G. Braun, A. Voigt, C. Neinhuis, C. Werner, *Langmuir* **2013**, *29*, 4 1100.

[50] J. Jurin, *Philosophical Transactions of the Royal Society of London* **1719**, *30*, 355 739.

[51] S. Dash, M. T. Alt, S. V. Garimella, *Langmuir* **2012**, *28*, 25 9606.